Original Article

Stress Block Parameters for Concrete Flexural Members Reinforced with Superelastic Shape Memory Alloys

Y.I. Elbahy

M.E.Sc. candidate, Department of Civil and Environmental Engineering,

The University of Western Ontario

London, Ontario, Canada, N6A 5B9

M.A. Youssef

Associate professor, Department of Civil and Environmental Engineering,

The University of Western Ontario

London, Ontario, Canada, N6A 5B9

M. Nehdi

Professor, Department of Civil and Environmental Engineering,

The University of Western Ontario

London, Ontario, Canada, N6A 5B9

Corresponding Author: **M.A. Youssef**

Email: youssef@uwo.ca,

Fax: 519-661-3779,

Phone: 519-661-2111, Ext: 88661

ABSTRACT

The unique properties of superelastic Shape Memory Alloys (SMAs) have motivated researchers to explore their use as reinforcing bars. The capacity of a steel Reinforced Concrete (RC) section is calculated by assuming a maximum concrete strain $\varepsilon_{c\text{-}max}$ and utilizing stress block parameters, α_1 and β_1, to simplify the nonlinear stress-strain curve of concrete. Recommended values for $\varepsilon_{c\text{-}max}$, α_1, and β_1 are given in different design standards. However, these values are expected to be different for SMA RC sections. In this paper, the suitability of using sectional analysis to evaluate the monotonic moment-curvature relationship for SMA RC sections is confirmed. A parametric study is then conducted to identify the characteristics of this relationship for steel and SMA RC sections. Specific mechanical properties are assumed for both steel and SMA. Results were used to judge on $\varepsilon_{c\text{-}max}$, α_1, and β_1 values given in the Canadian standard and to propose equations to estimate their recommended values for steel and SMA RC sections.

Keywords: reinforced concrete, shape memory alloys, moment-curvature relationship, stress block, ultimate concrete strain, moment capacity, axial load capacity.

INTRODUCTION

Although SMAs have many applications in different fields, they are considered relatively new to the civil engineering field. The shape memory effect, superelasticity, and performance under cyclic loading are unique properties that distinguish SMAs from other metals and alloys and make them attractive for various civil engineering applications. Some of these applications have been discussed by Wilson and Wesolowsky [1], DesRoches and Smith [2], Song et al. [3], Alam et al. [4], Janke et al. [5], and Li et al. [6, 7, 8]. This paper focuses particularly on one of these applications in which superelastic SMA bars are used to reinforce concrete structures.

While the constitutive relationship for SMA is a function of three parameters: stress, strain, and temperature, most of the widely used SMA models [9, 10, 11] are developed for quasi-static loading and are function of two parameters: stress and strain. The characteristic properties of the constitutive relationship are greatly affected by the strain rate [13, 14, 15]. This effect is not considered in the scope of this paper as monotonic behaviour is assumed. It needs to be considered when dynamic loads are examined.

Generally, SMA exhibit two distincit phases or crystal structures [15], Martensite (M-phase) and Austenite (A-phase). At the martensite phase, SMA has the ability to completely recover residual strains by heating (shape memory effect), while at the austenite phase, it recovers them upon unloading (superelasticity) [16].

The unique stress-strain relationship of superelastic SMA bars is expected to affect the moment-curvature (M-Φ) relationship of concrete sections. Thus values of α_1, and β_1 corresponding to a specific ε_{c-max} and used to evaluate the average concrete compressive stress and the location of the centroid of the compressive force are expected to be different for SMA RC sections. A23.3 [17] specifies a value of 0.0035 for ε_{c-max} and provides **Eqs. 1(a)** and **1(b)** to calculate α_1 and β_1 ($f_c^{'}$ is the concrete compressive strength). Moment capacity of a concrete section supporting an axial load P can be evaluated using plane section assumption and utilizing equilibrium as shown in **Fig. 1(a)**.

$$\alpha_1 = 0.85 - 0.0015\, f_c^{'} \qquad \geq 0.67 \qquad [1a]$$

$$\beta_1 = 0.97 - 0.0025 f_c^{'} \qquad \geq 0.67 \qquad [1b]$$

M-Φ analysis utilizing non-linear material constitutive models, **Fig. 1(b)**, can accurately determine the moment M_f and ultimate curvature Φ_u corresponding to ultimate concrete strain ε_{cu}, and $\varepsilon_{c\text{-}max}$ and Φ_{max} corresponding to the ultimate moment capacity M_u for a steel RC section [18]. In this paper, the validity of this method for SMA RC sections is confirmed. A parametric study is then conducted on concrete sections reinforced with either SMA or steel bars. The sections have different reinforcement ratio, dimensions, Axial Load Level $\left[ALI = \dfrac{P}{f_c^{'} \text{ x } A_g} \text{, where } A_g \text{ is the area of the concrete section} \right]$, and f'_c. The main features of the *M-Φ* relationship and normal force-moment interaction diagram for the studied SMA RC sections are identified considering monotonic loading. Based on the results of this study, A23.3 [17] values for $\varepsilon_{c\text{-}max}$, α_1, and β_1 are judged and new values are proposed.

RESEARCH SIGNIFICANCE

The use of superelastic SMA as reinforcing bars in concrete structures is expected to be implemented in the construction industry in the near future owing to the benefits provided by this smart material and the ongoing trend of reduction in its cost. The behaviour of SMA RC sections is currently not well understood, which can hinder the use of SMA in concrete structures. This study examines the monotonic behaviour of SMA RC concrete sections and provides key design parameters for steel and SMA RC sections. These parameters are only valid for cases when the mechanical properties for steel and/or SMA are similar to those used in the paper.

MATERIAL PROPERTIES

The model of Scott et al. [19] given by **Eq. 2** and shown in **Fig. 2(a)**, is used to model the stress-strain behaviour of concrete in compression. Concrete is assumed to crush when ε_{cu} reaches 0.0035 [17]. This value lies within the known range for unconfined concrete [20]. Concrete tensile resistance is ignored.

$$f_c = f_c'\left[2.0\left(\frac{\varepsilon_c}{0.002}\right)-\left(\frac{\varepsilon_c}{0.002}\right)^2\right] \qquad 0 \le \varepsilon_c \le 0.002 \qquad [2a]$$

$$f_c = f_c'\left[1 - Z(\varepsilon_c - 0.002)\right] \qquad \varepsilon_c \ge 0.002 \quad and \quad f_c \ge 0.2 f_c' \qquad [2b]$$

$$Z = \frac{0.5}{\dfrac{3+0.29 f_c'(\text{MPa})}{145 f_c'(\text{MPa}) - 1000} - 0.002} \qquad [2c]$$

Where: f_c = concrete compressive stress, Z = slope of compressive strain softening branch, ε_c = concrete compressive strain.

The stress-strain relationship for steel is assumed to be bilinear as shown in **Fig. 2(b)**. The material behaves elastically with a modulus of elasticity $E_{y\text{-}s}$ until the strain reaches $\varepsilon_{y\text{-}s}$. As the strain exceeds $\varepsilon_{y\text{-}s}$, the modulus of elasticity $E_{u\text{-}s}$ is significantly reduced to about 1 to 2% of $E_{y\text{-}s}$. Unloading at strains greater than $\varepsilon_{y\text{-}s}$ results in permanent deformations [20] as shown in Fig. 2(b).

Superelastic Ni-Ti alloys are the most suitable SMA for structural applications because of their high recoverable strain, durability, and being stable at the austenite phase at ambient temperature.

Ni-Ti stress-strain relationship consists of four linear branches that are connected by smooth curves. As a simplification, the smooth curves are ignored and the linear branches are assumed to intersect as shown in **Fig. 2(c)** [4, 21-26]. The alloy behaves elastically with a modulus of elasticity $E_{cr\text{-}SMA}$ until reaching the SMA critical stress $f_{cr\text{-}SMA}$ which represents the start of the martensite variant reorientation. As the strain ε_{SMA} exceeds the SMA critical strain $\varepsilon_{cr\text{-}SMA}$, the modulus of elasticity E_{p1} becomes 10% to 15% of $E_{cr\text{-}SMA}$. For strains above the martensite stress induced strain ε_{p1}, the material becomes stiffer and the modulus of elasticity E_{p2} reaches about 50 to 60% of $E_{cr\text{-}SMA}$. The final linear branch starts at the SMA yield point with a modulus of elasticity $E_{u\text{-}SMA}$ that is 3 to 8% of $E_{cr\text{-}SMA}$.

As shown in **Fig. 2(c)**, the SMA bar can recover its full deformations upon unloading if the strain ε_{SMA} is less than martensite stress induced strain ε_{p1} (superelasticity). If the strain exceeds ε_{p1}, permanent deformations will be obtained upon unloading. Full recovery of these deformations can be achieved through heating the SMA (shape memory effect) [21-26]. Reaching the yielding stress $f_{y\text{-}SMA}$ results in loosing the material superelasticity. For structural applications, it is recommended to design SMA RC sections to behave within the superelastic range [27]. Sections considered in this study will be designed such that it does not reach the real yielding. To simplify discussions and comparison with steel RC sections, the SMA critical stress is referred to as yielding in this paper.

SECTIONAL ANALYSIS

The methodology adopted for sectional analysis is similar to that used by Youssef and Rahman [28]. Assumptions for this method are plane sections remain plane and perfect bond exists between concrete and reinforcing bars. The method is based on using a fibre model. A section with width *b* and height *h* is divided into a finite number of layers as shown in **Fig. 2(d)**. Using the defined stress-strain models for steel, concrete, and SMA and taking into considerations section equilibrium and kinematics, the mechanical behaviour of the section can be analyzed for a given axial load and an increasing value of the applied moment.

EXPERIMENTAL VALIDATION

To validate the applicability of using sectional analysis for SMA RC sections, the behaviour of three small-scale superelastic SMA reinforced concrete beams tested by Saiidi et al. [29] was predicted numerically. The beams have the same dimensions but differ in their reinforcement ratio. All the beams have a span of 1270 mm, *b* of 127 mm, midspan *h* of 152 mm, and end *h* of 305 mm. The chemical composition of the used SMA bars as reported by Special Metals Corporation, USA is shown in **Table 1**. As the SMA rods had very low austenite phase starting temperature, the bars were cold drawn, thermally straightened to the superelastic condition, grit blasted, and heated at the ends. Details of the SMA reinforcement are given in **Table 2**.

Figures 3(a) and **3(b)** show the test setup and the cross-section of the tested beams. They were externally reinforced with SMA bars between the loading points and with regular steel reinforcing bars elsewhere. **Figure 3(c)** shows a typical SMA bar used in the beams. Saiidi et al. [29] indicated that their analytical predictions deviated from the experimental results because of the lack of bond between the concrete and the reinforcing bars and due to the variation of the diameter of the SMA bars. In this paper, the sectional analysis explained earlier is modified to account for the actual test setup.

The procedure used in the analysis in this section is similar to the procedure being used with unbonded tendons in prestressed concrete [30]. The procedure starts by assuming an average SMA bar strain $\varepsilon_{SMA\text{-}avg}$. Based on the length and cross-sectional area of the middle and two end parts of the SMA bar, their strains (ε_{mid}, and ε_{end}) are calculated. The force in the SMA bar is constant along its length and can be evaluated using ε_{mid} or ε_{end}. To satisfy section equilibrium, the compressive force in the concrete should be equal to the assumed tensile force. For a specific top compressive strain ε_{top}, the curvature Φ is iterated until equilibrium is satisfied. The corresponding moment is then calculated. The analysis is repeated for a range of top compressive strains ε_{top}. The relationship between the moment and the concrete strain at the location of the bar is established. The moment corresponding to the assumed $\varepsilon_{SMA\text{-}avg}$ is then obtained. This procedure is repeated for different values of $\varepsilon_{SMA\text{-}avg}$, which allows defining the M-Φ relationship. Analysis is terminated when ε_{top} reaches 0.0035.

It was clear from the load-average bar strain relationship reported by Ayoub et al. [31] that the strain in BNH2 exceeded ε_{p1}. As the stress-strain relationship for the Ni-Ti bars provided by Saiidi et al. [29] was bilinear, ε_{p1} and E_{p2} were assumed equal to 0.05 mm/mm, 22463 MPa, respectively. Moreover, it was observed that the neutral axis lies within the concrete section height at all load intervals. The low modulus of elasticity for SMA bars is the main factors that controlled the location of the neutral axis. **Figure 3(d)** shows the comparison between the analytical and experimental M-Φ diagrams for SMA reinforced beams. Very good agreement was observed for all specimens.

PARAMETRIC STUDY

A parametric study is conducted for typical concrete sections with different h (500 mm, 700 mm, and 900 mm), b (200 mm, 300 mm, and 400 mm), tensile reinforcement ratios ρ (0.25%, 0.50%, and 0.75%), compressive reinforcement ratios ρ' (0%, 0.125%, and 0.25%), f'_c (20 MPa, 40 MPa, and 60 MPa), and axial load levels (*ALI* ranges from 0 to 1). **Table 3** shows details of the analyzed sections. Each section is analyzed twice assuming that reinforcing bars are either SMA or steel with the mechanical properties given in **Table 4**. The mechanical properties of the used superelastic Ni-Ti are within the ranges provided by Alam et al. [4].

Because of the high value of $\varepsilon_{cr\text{-}SMA}$ (0.015 mm/mm), SMA bars did not exhibit tensile yielding at *ALI* higher than 0.2. In this paper, *ALI*=0 and 0.3 were chosen to present in details the behaviour of SMA RC sections. The results obtained for other *ALI* values were used to develop normal force-moment interaction diagrams. These diagrams were developed for both types of reinforcement, i.e. steel and SMA.

MOMENT–CURVATURE RESPONSE

Due to the difference in the modulus of elasticity of steel and SMA, the curvature $\Phi_{cr\text{-}SMA}$ corresponding to $f_{cr\text{-}SMA}$ for SMA RC sections was found to be higher than $\Phi_{y\text{-}s}$ for similar steel RC sections. The failure of SMA RC sections was initiated by crushing of concrete. Rupture of SMA bars did not govern failure because of the high ultimate tensile strain of the SMA bars (0.2 mm/mm). For steel RC sections, the failure type varied between concrete crushing and rupture of steel bars depending on section dimensions, reinforcement ratio, and axial load level. The effect of the different parameters on the M-Φ relationship is shown in **Figs. 4 to 8**. In these figures, the point at which the reinforcing bars reach f_{y-s} for steel or f_{cr-SMA} for SMA is marked by (y) and refereed to as yielding in the following paragraphs. The point at which the strain in the SMA bars exceeds ε_{p1} is defined by an (*H*). The two types of failure are defined by (*cc*) for concrete crushing and (*r*) for rupture of reinforcing bars.

Effect of cross-section height *h*

Figures 4(a) and 4(b) show the effect of varying *h* on the *M-Φ* relationship at two levels of axial load (*ALI*=0 and 0.3). At *ALI*=0, yielding of SMA RC sections occurred at higher curvature values (400% to 500%) than that for the steel RC sections. The ultimate curvature Φ_u of steel RC sections was found to decrease by 50% as *h* increased by 80%. This decrease is attributed to the failure type as it occurred by rupture of steel rather than crushing of concrete. The section ultimate curvature, Φ_u for SMA RC sections was not significantly affected by a similar increase in *h* since failure is governed by crushing of concrete.

Increasing the axial load level from 0 to 0.3 resulted in a significant increase (315%) in the cracking moment for both steel and SMA RC sections. Although the yielding moment M_y for steel RC sections increased with axial load increase, SMA RC sections did not exhibit yielding. The amount of strain energy calculated by integrating the area under the *M-Φ* relationship increased with the increase in *h* for both cases of reinforcement. At *ALI* of 0.3, SMA RC sections have similar initial stiffness, and their strain energy was comparable to that of steel RC sections.

Effect of cross-section width *b*

The effect of varying b on the M-Φ analysis is illustrated in **Figs. 5(a) and 5(b)**. At ALI=0, increasing b had a minor effect on M_y and M_u for both steel and SMA reinforcement. Although Φ_u was not affected for steel RC sections, Φ_u for SMA RC sections increased by 90% as b increased by 100%. This increase in Φ_u resulted in 125% increase in the strain energy.

At higher axial load level (ALI=0.3), **Fig. 5(b)**, the curves for SMA and steel RC sections coincided prior to cracking. For both types of RC sections, Φ_u was not affected by changing b and a significant increase, about 80%, in section capacity was achieved by increasing b by 100%. Although SMA bars did not exhibit any yielding for the studied sections, their strain energy reached values as high as 9665 N.rad. M_y for steel RC sections increased by 200% to 400% due to the increase in the axial load level. The increase in the axial load level decreased the strain energy by about 60% for both types of reinforcement.

Effect of tensile reinforcement ratio *ρ*

As shown in **Fig. 6(a)** (ALI=0), a 200% increase in ρ increases the section capacity by 160% for both types of reinforcement. Although M_y increased with increasing ρ, the yielding curvature was slightly affected. The increase in ρ resulted in decreasing Φ_u. For lower reinforcement ratio (ρ=0.25%), the strain energy for SMA RC sections was 45% higher than that of steel RC sections since SMA bars exhibited extensive yielding. As ρ increased, the strain energy became higher for steel RC sections.

At higher levels of axial load, ALI=0.3, the effect of increasing ρ on increasing the section capacity is higher for steel RC sections, **Fig. 6(b)**. Increasing ALI from 0 to 0.3 increased the cracking moment by 320%. Failure occurred by crushing of concrete and thus Φ_u was not affected. The strain energy for steel RC sections was 11% higher than SMA RC sections.

Effect of compressive reinforcement ratio ρ'

Figure 7(a) represents the M-Φ relationship for SMA and steel RC sections for different values of ρ'. At ALI=0, ρ' has no effect on M_y, Φ_u, and M_u. Failure for steel RC sections occurred by rupture of steel. As the SMA bars exhibited higher yielding than that of the steel bars, the strain energy and section ultimate curvature Φ_u were higher for SMA RC sections than for steel RC sections.

Increasing ALI from 0 to 0.3 resulted in higher section capacity for both types of reinforcement, **Fig. 7(b)**. ρ' was found to slightly affect the section capacity. M_y was also slightly affected for steel RC sections. SMA RC sections did not exhibit yielding at this level of axial load. Failure occurred by crushing of concrete for both SMA and steel RC sections. This type of failure resulted in almost equal Φ_u for the analyzed sections. The strain energy for steel RC sections was 12% to 23% higher than SMA RC sections.

Effect of concrete compressive strength f_c'

At ALI=0, **Fig. 8(a)**, increasing f'_c from 20 to 40 MPa did not notably affect M_y or M_u for both types of reinforcement. For steel RC sections, failure occurred by rupture of reinforcing bars and thus Φ_u was almost constant. However, for SMA RC sections, Φ_u increased by 90% with the increase of f'_c . At f'_c=60 MPa, the yielding plateau of SMA bars was followed by a strain hardening behaviour resulting in a substantial increase in section capacity and ductility.

At *ALI*=0.3, **Fig. 8(b)**, the cracking and ultimate moments for both types of reinforcement increased by 160% to 180%. Increasing f'_c from 20 MPa to 60 MPa resulted in an increase of 155% in the yielding moment for the steel RC sections. SMA bars did not yield at this level of axial load. Φ_u was comparable for SMA and steel RC sections since failure occurred by crushing of concrete.

NORMALIZED INTERACTION DIAGRAMS

As mentioned earlier, the *M-Φ* analysis was conducted at different *ALI*. The obtained values for M_u at different *ALI* were used to develop the normal fprce-moment interaction diagrams that are shown in **Figs. 9** to **11**. For each analyzed section, $\varepsilon_{c\text{-}max}$ and Φ_{max} corresponding to the peak moment M_u were identified.

The point at which the interaction diagrams of steel RC sections change the sign of their slope is known as the balance point. It is the point at which steel yields ($\varepsilon_{y\text{-}s}$=0.0022) simultaneously with concrete reaching its crushing strain (ε_{cu} =0.0035). For the analyzed sections, the balance point occurred at an axial load level *ALI* ranging from 0.3 to 0.5. The difference in the stress-strain relationship between steel and SMA resulted in a different behaviour for SMA RC sections. The point at which the curve changed the sign of its slope was not related to yielding of SMA bars. It occurred at an axial load level close to that for steel RC sections (*ALI*=0.3 to 0.5). At this point, SMA bars did not yield and $\varepsilon_{c\text{-}max}$ varied from 0.00261 to 0.0031.

Effect of cross-section height *h*

Figure 9(a) illustrates the effect of varying h on the interaction diagrams. The pure flexural capacity $\left[\frac{P}{A_g}=0\right]$ was the most affected point. As the axial load level increased on the section, the effect of varying h on section capacity decreased. The pure axial capacity was slightly higher (3%) for SMA RC sections than for the steel ones because of the higher yielding stress of the SMA bars. This increase was noticed for all other cases.

Effect of cross-section width *b*

As shown in **Fig. 9(b)**, varying b has a clear effect on the interaction diagram for both steel and SMA reinforcement. The pure flexural capacity, where the axial load is zero, changed by about 50% when b increased from 200 mm to 400 mm. Varying b from 200 mm to 300 mm did not affect the interaction diagrams at high levels of axial load (ALI>0.5). However, increasing b from 300 mm to 400 results in a clear effect on section capacity at all levels of axial load.

Effect of tensile reinforcement ratio *ρ*

The interaction diagrams shown in **Fig. 10(a)** represent the effect of varying ρ on the section capacity. At low levels of axial loads (ALI<0.4), increasing the reinforcement ratio ρ from 0.25% to 0.75% resulted in a significant increase (140% for steel - 165% for SMA) in section capacity. For ALI>0.4, the effect of increasing ρ was reduced as failure was governed by crushing of concrete rather than rupture of steel.

Effect of compressive reinforcement ratio ρ'

As shown in **Fig. 10(b)**, the interaction diagrams for steel RC sections were affected more by varying ρ' than SMA RC sections. The pure flexural capacity was not affected significantly by varying the reinforcement ratio ρ' for both steel and SMA reinforcement. At *ALI*=0.4, the capacity of steel RC sections increased by 11% as ρ' increased from 0 to 0.25%.

Effect of concrete compressive strength f_c'

It can be observed from **Fig. 11** that increasing f'_c significantly increases the section capacity. The pure flexural capacity increased by 35% by changing f'_c from 20 MPa to 60 MPa, and the section capacity at higher axial load levels (i.e. *ALI*=0.4) drastically increased (195%). The pure axial capacity (*M*=0) also increased significantly (185%) with increase in f'_c of 200%.

RECTANGULAR STRESS BLOCK PARAMETERS

Building codes provide engineers with equivalent stress block parameters α_1 and β_1 to simplify the design process. The use of α_1, and β_1 allows calculating the concrete compressive force and its location. A23.3 [17] equations for calculating α_1, and β_1, **Eq. 1**, are dependent on f_c' to account for the difference in behaviour of high strength concrete (f_c' > 60 MPa).

In this section, and for each of the analyzed sections, α_1 and β_1 were calculated from the known strain distribution at the peak moments. The compressive force in concrete C_c and its point of application are evaluated by calculating the area under the stress-strain relationship of concrete corresponding to the known ε_{c-max}, and Φ_{max}, and its centroid. The stress block parameters are then found such that they result in the same area and same location of the centroid. In addition, the Canadian code recommended values have been judged for steel RC sections.

Steel RC sections

Figure 12(a) shows the variation of ε_{c-max} with the axial load level for steel RC sections. At *ALI*=0, failure occurred in some of the considered sections by rupture of the reinforcement, before ε_{c-max} reaches its limit of 0.0035. As a result, ε_{c-max} varied between 0.0020 and 0.0035. For $0 \leq ALI \leq 0.1$, failure occurred at $\varepsilon_{c-max} = 0.0035$. ε_{c-max} started to decrease with *ALI* increase approaching a value of 0.002 at *ALI*=1.0. This behaviour is similar to the recommendation of the Eurocode [32] where the value for the limiting concrete compressive strain is a function of the load eccentricity. A value of 0.0035 is recommended for flexural and for combined bending and axial load where the neutral axis remains within the section. For other sections (neutral axis outside the section), a value between 0.0035 and 0.002 is to be used.

From the parametric study conducted in this paper, it is recommended to calculate ε_{c-max} as a function of *ALI*. ε_{c-max} can be assumed equal to 0.0035 for $ALI \leq 0.1$, 0.0028 for $0.2 \leq ALI \leq 0.5$, and 0.002 for *ALI*=1.0. Linear interpolation can be used for different *ALI* values. The recommended values for ε_{c-max} are shown on **Fig. 12(a)**.

Figures 12(b) and **12(c)** show the variation of α_1 and β_1 with ε_{c-max}. α_1 is found to approach a value of 1.0 at ε_{c-max} of 0.002 (pure axial load). Based on the analytical results, **Eqs. 3** and **4** were developed to calculate α_1, and β_1 based on ε_{c-max}. The predictions of these equations are shown in **Figs. 12(b)** and **12(c).**

$$\alpha_1 = 88.36\times10^3\ \varepsilon_{c-\max}^2 - 552.4\,\varepsilon_{c-\max} + 1.750 \qquad 0.002 \le \varepsilon_{c-\max} \le 0.00275 \qquad [3a]$$

$$\alpha_1 = -33.54\times10^3\ \varepsilon_{c-\max}^2 + 150.7\,\varepsilon_{c-\max} + 750.0\times10^{-3} \qquad 0.00275 \le \varepsilon_{c-\max} \le 0.0035 \qquad [3b]$$

$$\beta_1 = -1630\times10^3\ \varepsilon_{c-\max}^2 + 8388\,\varepsilon_{c-\max} - 10.00 \qquad 0.002 \le \varepsilon_{c-\max} \le 0.00275 \qquad [4a]$$

$$\beta_1 = -5513\,\varepsilon_{c-\max}^2 + 114.1\,\varepsilon_{c-\max} + 540.0\times10^{-3} \qquad 0.00275 \le \varepsilon_{c-\max} \le 0.0035 \qquad [4b]$$

The capacity of the analyzed sections were calculated based on the values of ε_{c-max}, α_1, and β_1 recommended in the previous sections and based on A23.3 [17] recommended values. **Fig. 12(d)** shows a comparison of the calculated values and the exact values obtained using the *M-Φ* analysis. The proposed values resulted in very good agreement, maximum error equal to 5%. The recommended values by A23.3 [17] were found to significantly underestimate the section capacity at high levels of axial load.

SMA RC sections

For SMA RC sections, ε_{c-max} is found to be dependent on the axial load level *ALI* as shown in **Fig. 13(a)**. It is recommended to assume ε_{c-max} equal to 0.0035 for $ALI \le 0.2$, 0.00275 for ALI=0.4, 0.00255 for ALI=0.6, and 0.002 for ALI=1.0. Linear interpolation can be used for different *ALI* values.

Figures 13(b) and **13(c)** show the variation of α_1 and β_1 with ε_{c-max}. Based on these figures, **Eqs. 5** and **6** were developed to calculate α_1 and β_1. The square value of the coefficient of determination R^2 corresponding to these equations ranges between 0.9922 and 0.9999.

$$\alpha_1 = 182.7\times10^3\ \varepsilon_{c-\max}^2 - 982.1\,\varepsilon_{c-\max} + 2.240 \qquad 0.002 \le \varepsilon_{c-\max} \le 0.00275 \qquad [5a]$$

$$\alpha_1 = -24.62\times10^3\ \varepsilon_{c-\max}^2 + 94.05\,\varepsilon_{c-\max} + 840.0\times10^{-3} \qquad 0.00275 \le \varepsilon_{c-\max} \le 0.0035 \qquad [5b]$$

$$\beta_1 = -1477\times10^3\ \varepsilon_{c-\max}^2 + 7719\,\varepsilon_{c-\max} - 9.280 \qquad 0.002 \le \varepsilon_{c-\max} \le 0.00275 \qquad [6a]$$

$$\beta_1 = -5867\,\varepsilon_{c-\max}^2 + 116.4\,\varepsilon_{c-\max} + 540.0\times10^{-3} \qquad 0.00275 \le \varepsilon_{c-\max} \le 0.0035 \qquad [6b]$$

The accuracy of the estimated values for ε_{c-max}, α_1, and β_1 was checked by calculating the capacity based on the proposed values (**Eqs. 5** and **6**). **Figure 13(d)** shows the relationship between the normalized ultimate moment M_u obtained from the M-Φ analysis versus the normalized moment M_r obtained based on the recommended values of ε_{c-max}, α_1, and β_1. The maximum error in M_r is 2% for $ALI < 0.5$, and 6% for ALI ranges from 0.6 to 0.9. The error for sections with compression reinforcement was higher. The normalized moment M_{code} calculated based on the recommended values by A23.3 [17] were also plotted versus the normalized ultimate moment M_u obtained from the M-Φ analysis, **Fig. 13(d)**. A23.3 [17] recommended values were found to be conservative in calculating the section capacity at all levels of axial load. At high ALI, A23.3 [17] recommended values were found to significantly underestimate the section capacity.

SUMMARY AND CONCLUSIONS

This study investigates the flexural behaviour of SMA RC sections as compared to steel RC sections. The accuracy of using sectional analysis for SMA RC sections was validated by comparing analytical predictions and experimental results for three simply supported beams. Sectional analysis was modified to account for the test setup that included using external unbonded superelastic SMA bars.

A number of steel and SMA RC sections were then chosen. Variables were section height and width, tensile and compressive reinforcement ratios, concrete compressive strength, and axial load level. For each section, the M-Φ relationship was established and used to evaluate the moment capacity M_u, the corresponding curvature Φ_{max}, and maximum concrete strain ε_{c-max}. Based on the results of the parametric study, the following conclusions can be drawn.

Moment-curvature relationship:

At ALI=0, SMA RC sections have lower initial stiffness than steel RC sections. The difference in the initial stiffness vanishes for higher ALI as the axial load delays cracking of the section. Although SMA bars did not yield at ALI>0.2, SMA RC sections strain energy had values comparable to that of steel RC sections.

Steel RC sections failed either by rupture of steel bars or concrete crushing at low axial load levels and by concrete crushing at high ALI. SMA RC sections failed by concrete crushing rather than rupture of SMA bars because of their high tensile strain. For higher concrete compressive strength, sections with low area of SMA bars exhibited a strain hardening following the initial yielding. This behaviour might not be acceptable as the strain in the SMA bars exceeded their recovery strain, which defeat the purpose of using them.

Normal force-moment interaction diagrams

The change in the sign of the slope of steel RC interaction diagrams happens at the balanced moment. This point is defined as the point at which the steel yields in tension and the concrete crushes in compression. For SMA RC sections, the point at which the sign changes is not related to yielding of SMA bars. It happens as a result of the change in the maximum concrete strain and the compression zone height. It was also observed that the pure axial capacity of SMA RC sections is higher than that of steel RC sections due to the higher yield stress for SMA bars.

Stress block parameters

The maximum concrete strain $\varepsilon_{c\text{-}max}$ for steel RC sections was found to be equal to 0.0035 for *ALI* between 0 and 0.1. This correlates well with the Canadian standards. However, for *ALI*=0, $\varepsilon_{c\text{-}max}$ was found to deviate from this value because of the change in the failure mode from compression failure to reinforcement rupture. This change was discussed by other researchers and found to have minor effect on the calculations of the moment capacity. Another deviation was observed at *ALI* exceeding 0.1. It is proposed to assume $\varepsilon_{c\text{-}max}$ equal to 0.0035 for ALI ≤ 0.1, 0.0028 for 0.2 ≤ *ALI* ≤ 0.5, and 0.002 for *ALI*=1.0. Linear interpolation can be used for different *ALI* values. The corresponding values for α_1, and β_1 are proposed.

For SMA RC sections, it was found that ε_{c-max} can be assumed 0.0035 for $ALI \leq 0.2$, 0.00275 for ALI=0.4, 0.00255 for ALI=0.6, and 0.002 for ALI=1.0. For other ALI values, ε_{c-max} is proposed to be evaluated by linear interpolation. Two equations were developed to calculate α_1, and β_1 for SMA RC sections.

The accuracy of the proposed values of ε_{c-max}, α_1, and β_1 for steel and SMA RC sections was validated by comparing the moment capacity calculated based on these parameters and that obtained from the moment-curvature relationships. The equations provided good estimates of the moment capacity and were found to be superior to the equations proposed by the Canadian code.

<u>The conclusions reached in this paper are based on the properties assumed for steel and SMA bars. For other properties, the validity of the proposed values and the proposed equations needs to be checked.</u>

REFERENCES

1. Wilson, J.C. and Wesolowsky, M.J. (2005) Shape memory alloys for seismic response modification: A state-of-the-art review. Earthquake Spectra 21: 569-601.

2. DesRoches, R., and Smith, B. (2004) Shape memory alloys in seismic resistant design and retrofit: a critical review of their potential and limitations. Journal of Earthquake Engineering 8: 415-429.

3. Song, G., Ma, N., and Li, H.-N. (2006) Application of shape memory alloys in civil structures. Engineering Structures 28: 1266-1274.

4. Alam M.S., Youssef M.A., Nehdi, M. (2007) Utilizing shape memory alloys to enhance the performance and safety of civil infrastructure: a review. Canadian Journal of Civil Engineering 34(9): 1075-1086.

5. Janke, L., Czaderski, C., Motavalli, M., Ruth, J. (2005) Applications of shape memory alloys in civil engineering structures – overview, limits, and new ideas. Materials and Structures, 38(5): 578-592.

6. Li, H., Liu, Z., and Ou, J. (2007) Study on reinforced concrete beams strengthened using shape memory alloy wires in combination with carbon-fiber-reinforced polymer plates. Smart Materials and Structures, 16(6): 2550-2559.

7. Li, H., Liu, Z., and Ou, J. (2006) Behavior of a simple concrete beam driven by shape memory alloy wires. Smart Materials and Structures, 15: 1039-1046.

8. Li, H., Liu, Z., Li, Z., and Ou, J. (2004) Study on damage emergency repair performance of a simple beam embedded with shape memory alloys. Advances in Structural Engineering, 7(6): 495-502.

9. Tanaka, K. (1986) A thermomechanical sketch of shape memory effect: One-Dimensional tensile behavior. Res. Mechanica, 18:251–263.

10. Brinson, L. (1990) One-dimensional constitutive behavior of shape memory alloys: thermo mechanical derivation with non-constant material functions. Journal of Intelligent Materials and Structures, 1:207–234.

11. Liang, C., and Rogers, C. (1990) One-dimensional thermo mechanical constitutive relations for shape memory material. Journal of Intelligent Materials and Structures, 1:207–234.

12. Prahlad, H., and Chopra, I. (2001) Experimental characteristics of Ni- Ti shape memory alloys under uniaxial loading conditions. Journal of Intelligent Material Systems and Structures, 11(4):272–282.

13. Gadaj, S., Nowacki, W., Pieeczyska, E. and Tobushi, H. (1999) Temperature evolution during tensile test of shape memory alloy. Archives of Mechanics, 51(6):649–663.

14. McCormick, P.G., Liu, Y. and Miyazaki, S. (2001) Intrinsic thermal-mechanical behavior associated with the stress-induced martensitic transformation of NiTi. Material Science and Engineering, 167:51–56.

15. DesRoches, R., McCormick, J., and Delemont, M. (2004) Cyclic properties of superelastic shape memory alloy wires and bars. Journal of structural Engineering, ASCE, 130(1): 38–46.

16. Otsuka, K., and Wayman, C. M. (1998) Mechanism of shape memory effect and superplasticity. Shape memory materials, K. Otsuka and C. M. Wayman, eds., Cambridge University Press, Cambridge, U.K., 27–48.

17. A23.3 (2004) Design of concrete structures. Canadian Standards Association, Mississauga, ON, 358 pp.

18. Ozbakkalogln T., and Saatcioglu M. (2004) Rectangular Stress Block for High-Strength Concrete. ACI Structural Journal 101(4): 475 - 483.

19. Scott, B.D.; Park, R.; and Priestley, M.J.N. (1982) Stress-strain behavior of concrete confined by overlapping hoops at low and high strain rates. ACI journal, Proceedings 79(1): 13-27.

20. Park R., Paulay T. (1975) Reinforced concrete structures. John Wiley & sons, New York.

21. Manach, P.-Y., and Favier, D. (1997) Shear and tensile thermomechanical behavior of near equiatomic NiTi alloy. Materials Science & Engineering A: Structural Materials: Properties, Microstructure and Processing. A222: 45-57.

22. Zak, A.J., Cartmell, M.P., Ostachowicz, W.M. and Wiercigroch, M. (2003) One-dimensional shape memory alloy models for use with reinforced composite structures. Smart Materials and Structures 12(3): 338-346.

23. DesRoches, R., McCormick, J., and Delemont, M. (2004) Cyclic properties of superelastic shape memory alloy wires and bars. Journal of Structural Engineering, ASCE 130(1): 38-46.

24. Otsuka, K. and Wayman, C.M. (1999) Shape memory materials. 1st Paperback Edition, Cambridge University Press, Cambridge.

25. Liu, Y., Xie, Z., Humbeeck, J.V. and Delaey, L. (1998) Asymmetry of stress–strain curves under tension and compression for NiTi shape memory alloys. Acta Materialia 46(12): 4325-4338.

26. Orgeas, L., and Favier, D. (1995) Non-symmetric tension-compression behavior of NiTi alloy. Journal De Physique, IV: JP 5(8): 605-610.

27. Youssef, M.A., Alam, M.S., Nehdi, M. "Experimental Investigation on the Seismic Behaviour of Beam-Column Joints Reinforced with Superelastic Shape Memory Alloys." In-press, Journal of Earthquake Engineering, accepted January 2008.

28. Youssef, M.A., and Rahman, M. (2007) Simplified seismic modeling of reinforced concrete flexural members. Magazine of Concrete Research 59(9): 639-649.

29. Saiidi,M.S., Sadrossadat-Zadeh, M., Ayoub,C., Itani,A. (2007) Pilot study of behavior of concrete beams reinforced with shape memory alloys. Journal of Materials in Civil engineering, American Society of Civil Engineers, 19(6): 454-461.

30. Collins, M.P., and Mitchell, D. (1991) Prestressed concrete structures. Prentice-Hall, Englewood Cliffs, N.J., 766 pp.

31. Ayoub, C., Saiidi, M., and Itani, A. A study of shape-memory alloy-reinforced beams and cubes. *Rep. No. CCEER-03-7*, Center for Civil Engineering Earthquake Research, Dept. of Civil Engineering, Univ. of Nevada, Reno, Nevada.

32. Beeby, A.W., and Narayanan, R.S. (2005) Designers' guide to EN 1992-1-1 and EN 1992-1-2 : Eurocode 2: design of concrete structures : general rules and rules for buildings and structural fire design. Thomas Telford, London.

List of notations:

$\overline{Y}$	Distance between point of action of the concrete compressive force and the centroidal axis.
A'_s	Compressive reinforcement area.
A_g	Gross area of concrete section.
ALI	Axial load index which represents the ratio between the applied axial load to the axial capacity of the cross-section.
A_s	Tensile reinforcement area.
b	Cross-section width.
C	Compression zone height.
C_c	Compressive force in concrete.
cc	Point at which concrete reaches its crushing strain.
$E_{cr\text{-}SMA}$	SMA modulus of elasticity before the start of martensite variant reorientation (austenite phase).
E_{p1}	SMA modulus of elasticity before the start of the stress induced martensite phase.
E_{p2}	SMA modulus of elasticity after the start of the stress induced martensite phase (martensite phase).
$E_{u\text{-}s}$	Steel plastic modulus of elasticity.
$E_{u\text{-}SMA}$	SMA post-yielding modulus of elasticity.
$E_{y\text{-}s}$	Steel elastic modulus of elasticity.
f'_c	Concrete compressive strength.
f_c	Concrete compressive stress.
$f_{cr\text{-}SMA}$	SMA critical stress (start of martensite variant reorientation).
f_{p1}	Martensite stress induced stress.
f_s	Steel stress.
$f_{u\text{-}s}$	Steel ultimate stress.
$f_{u\text{-}SMA}$	SMA ultimate stress.
$f_{y\text{-}s}$	Steel yielding stress.
$f_{y\text{-}SMA}$	SMA yielding stress.
h	Cross-section height.
H	Point at which strain in the SMA bars exceeds ε_{p1}.
M	Moment.
M_{code}	Moment obtained using A23.3 [17] recommended values (Equation1).
M_f	The failure moment.
M_r	Moment obtained using the proposed equations for α_1, and β_1.
M_u	Ultimate moment.
M_y	Yielding moment.
NSC	Normal strength concrete.
P	Axial load.

R	Coefficient of determination.
r	Point at which rupture of reinforcing bars occurs.
T_s	Tensile force in the SMA bars.
y	Point at which bars reach f_{y-s} for steel or for f_{cr-SMA} SMA.
Z	Slope of compressive strain softening branch.
α_1 , β_1	Stress block parameters.
ε_c	Concrete compressive strain.
ε_{c-max}	Concrete maximum strain corresponding to the peak moment.
ε_{cr-SMA}	SMA critical strain.
ε_{cu}	Ultimate concrete compressive strain.
ε_{end}	End part of the bar strain.
ε_{mid}	Middle part of the bar strain.
ε_{p1}	Martensite stress induced strain.
ε_{SMA}	SMA strain.
$\varepsilon_{SMA-avg.}$	SMA average bar strain.
ε_{top}	Concrete top compressive strain.
ε_{u-s}	Steel strain at failure.
ε_{u-SMA}	SMA strain at failure.
ε_{y-s}	Steel yielding strain.
ε_{y-SMA}	SMA yielding strain.
ρ	Tensile reinforcement ratios.
ρ'	Compressive reinforcement ratios.
Φ	Curvature.
Φ_{cr-SMA}	Curvature corresponding to the SMA critical stress.
Φ_{max}	Curvature corresponding to the peak moment.
Φ_u	Ultimate curvature.
Φ_{y-s}	Curvature corresponding to the steel yielding stress.

TABLES AND FIGURES

List of Tables:

List of Figures:

Fig. 12: Steel RC sections. (a) $\varepsilon_{c\text{-}max} – ALI$ relationship. (b) $\alpha_1 – \varepsilon_{c\text{-}max}$ relationship. (c) $\beta_1 – \varepsilon_{c\text{-}max}$ relationship. (d) M_r / ($\mathrm{A_g}$ x h) – M_u / (A_gx h) relationship.

Fig. 13: SMA RC sections. (a) $\varepsilon_{c\text{-}max} – ALI$ relationship. (b) $\alpha_1 – \varepsilon_{c\text{-}max}$ relationship. (c) $\beta_1 – \varepsilon_{c\text{-}max}$ relationship. (d) M_r / ($\mathrm{A_g}$ x h) – M_u / (A_gx h) relationship.

Table 1 – Chemical Composition of the SMA rods.

Element	Weight %
Nickel Titanium	55.90 44.01%
Oxygen	257 ppm
Carbon	374 ppm
Cu, Cr, Co, Mn, Mo, W, V	< 0.01
Nb, Al, Zr, Si, Ta, Hf	< 0.01
Ag, Pb, Bi, Ca, Mg, Sn, Cd	< 0.01
Zn, Sb, Sr, Na, As, Be, Ba	< 0.01
Fe	< 0.05
B	< 0.001
Hydrogen	14 ppm

Table 2 – Properties of tested beams.

Specimen	Midspan SMA reinforcement	$\varepsilon_{y\text{-}SMA}$ (mm/mm)	$f_{y\text{-}SMA}$ (MPa)	$E_{y\text{-}SMA}$ (MPa)
BNL2	2 Φ 6.40 mm	0.013	400	34078
BNH1	1 Φ 9.50 mm	0.013	510	39245
BNH2	2 Φ 9.50 mm	0.013	510	39245

Table 3 – Details of analyzed sections.

Section	Studied variables	h (mm)	b (mm)	A_s (mm^2)	A'_s (mm^2)	f'_c (MPa)
C_1	h	500	300	655	0	40
C_2	b, h	700	300	655	0	40
C_3	h	900	300	655	0	40
C_4	b	700	200	655	0	40
C_5	b	700	400	655	0	40
C_6	ρ, ρ', f'_c	700	300	525	0	40
C_7	ρ	700	300	1050	0	40
C_8	ρ	700	300	1575	0	40
C_9	ρ'	700	300	525	262.5	40
C_{10}	ρ'	700	300	525	525.0	40
C_{11}	f'_c	700	300	525	0	20
C_{12}	f'_c	700	300	525	0	60

Table 4 – Mechanical properties of SMA and steel bars.

Material	Property	E_y (GPa)	f_y (MPa)	f_{p1} (MPa)	f_u (MPa)	ε_{p1} (%)	ε_u (%)
SMA	Tension	36	540	600	1400	7.0	20
	Compression	60	650	735	1500	4.5	20
Steel	Tension or Compression	200	438	NA	615	NA	3.5

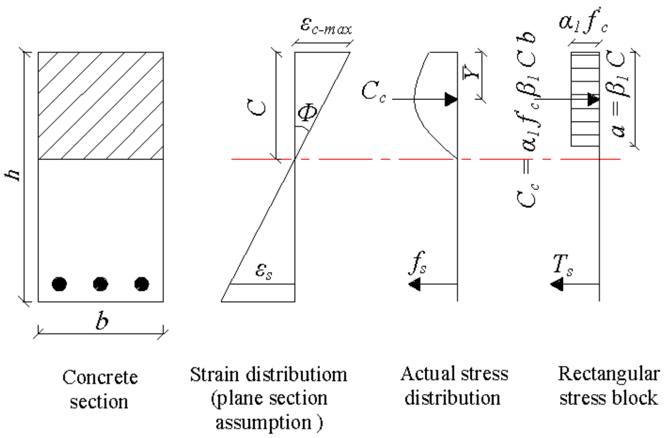

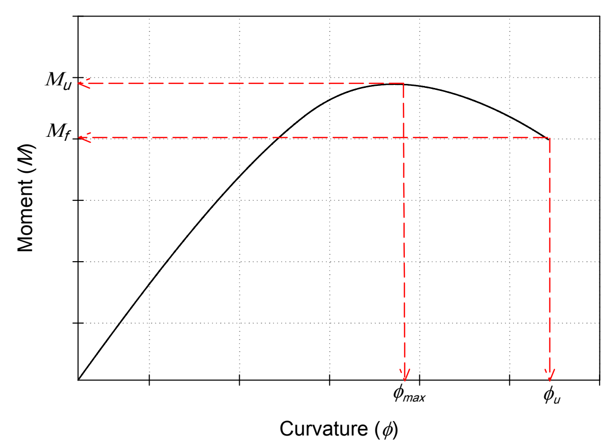

(a) Stress block parameters for rectangular sections.

(b) Typical *M-Φ* relationship.

Fig. 1

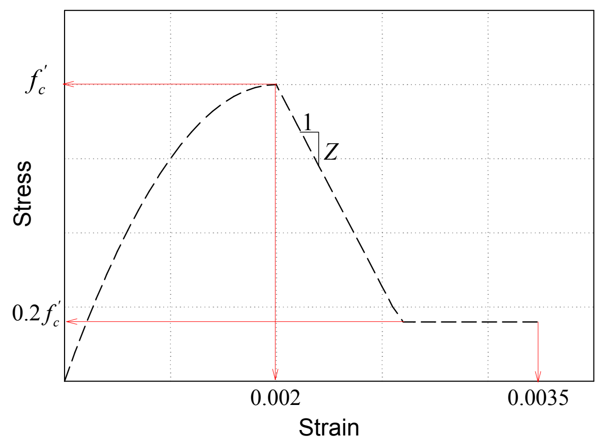

(a) Stress-strain model for concrete in compression.

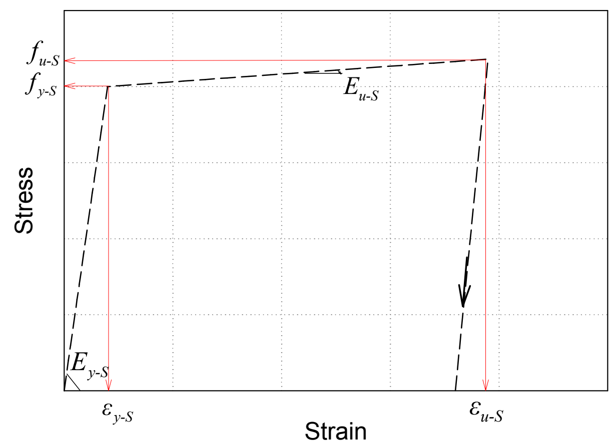

(b) Stress-strain model for steel.

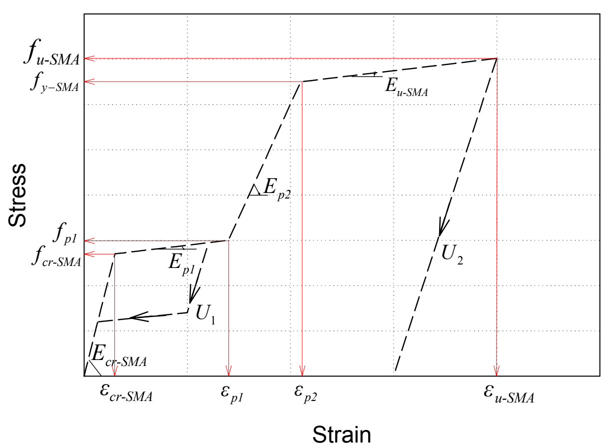

(c) Stress-strain model for SMA.

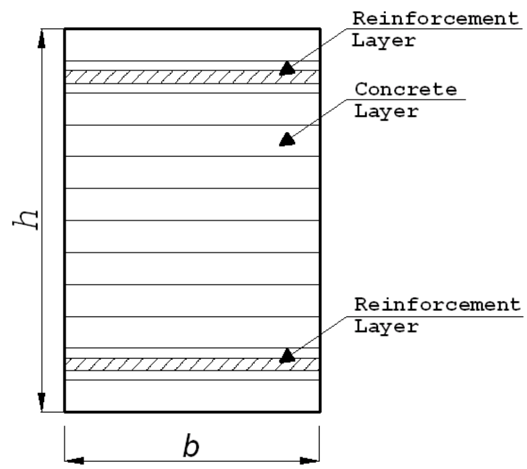

(d) Fibre model for a concrete section.

Fig. 2

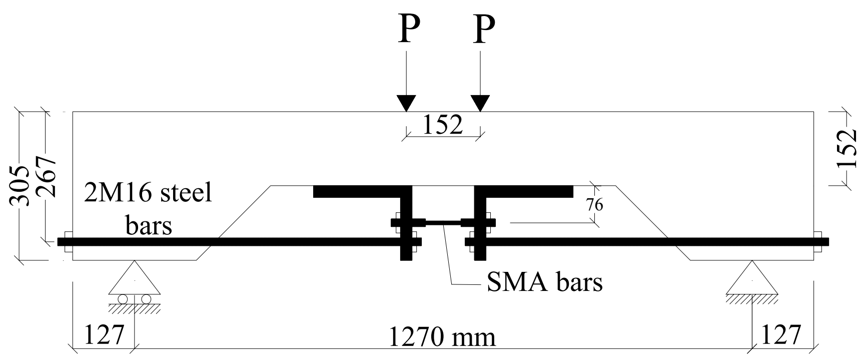

(a) Details of the tested beam.

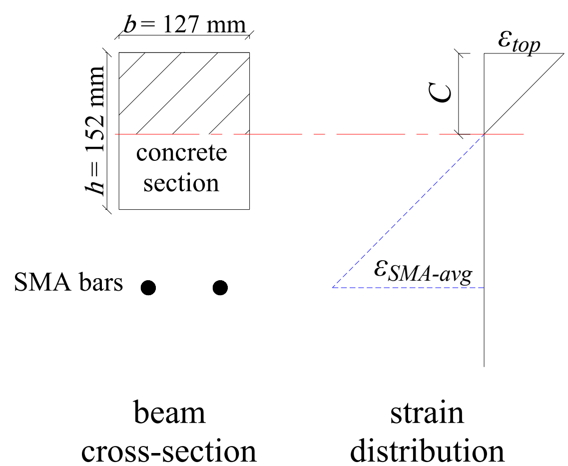

(b) Beam mid-span cross-section.

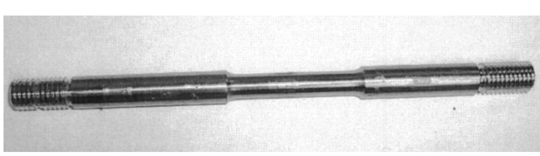

(c) SMA typical bar (Saiidi et al. [28] after permission).

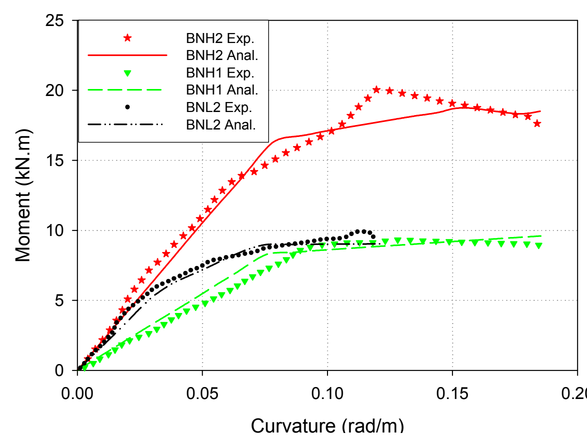

(d) Experimental versus analytical moment-curvature for SMA reinforced beams.

Fig. 3

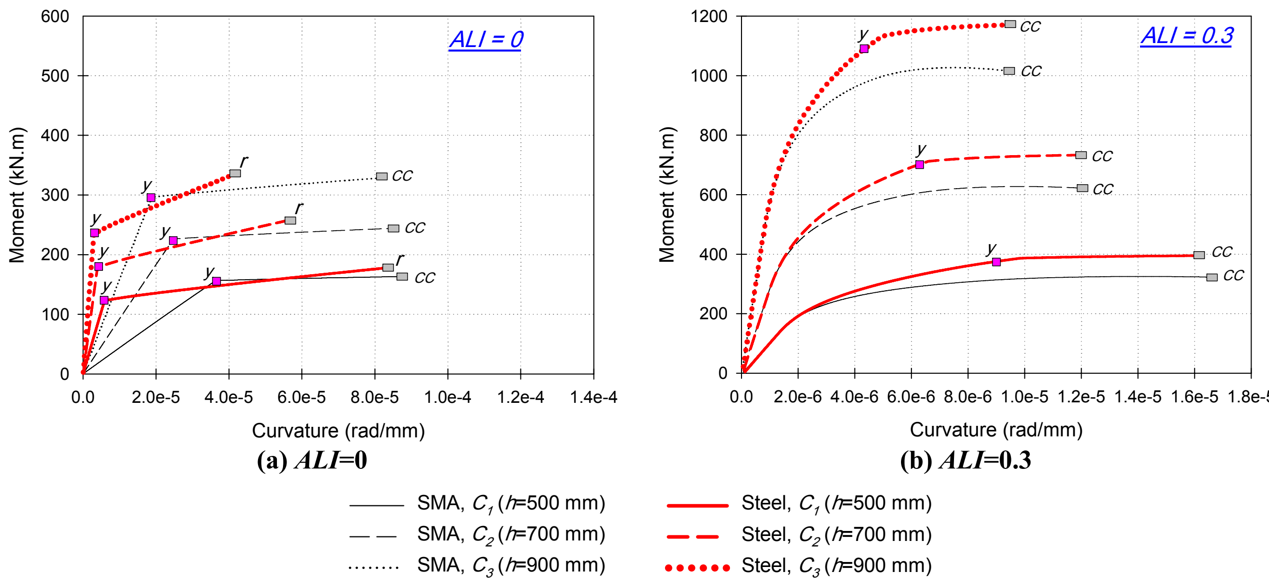

Fig. 4: Effect of varying *h* on the *M*-*Φ* relationship.

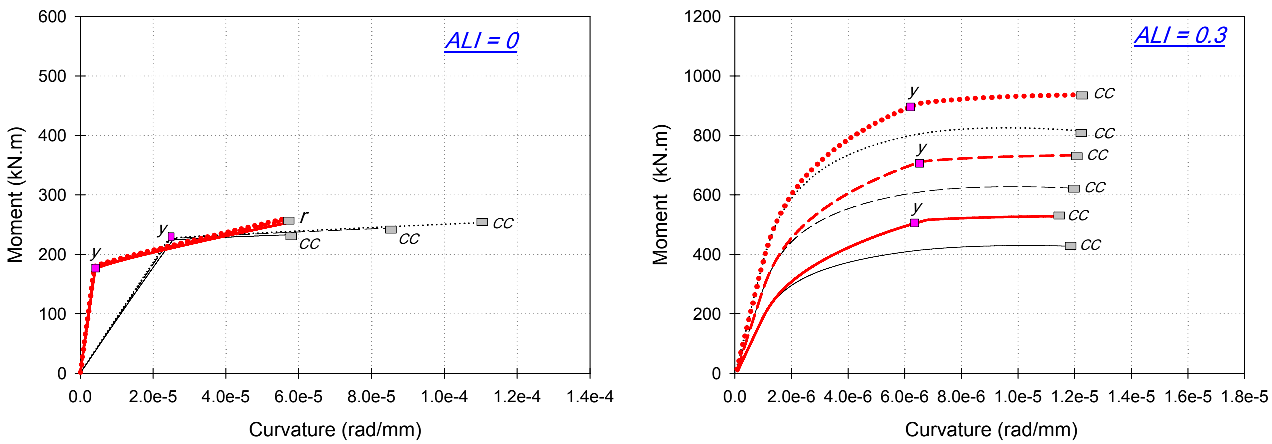

(a) *ALI*=0. **(b) *ALI*=0.3.**

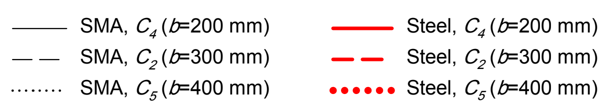

Fig. 5: Effect of varying *b* on the *M*-*Φ* relationship.

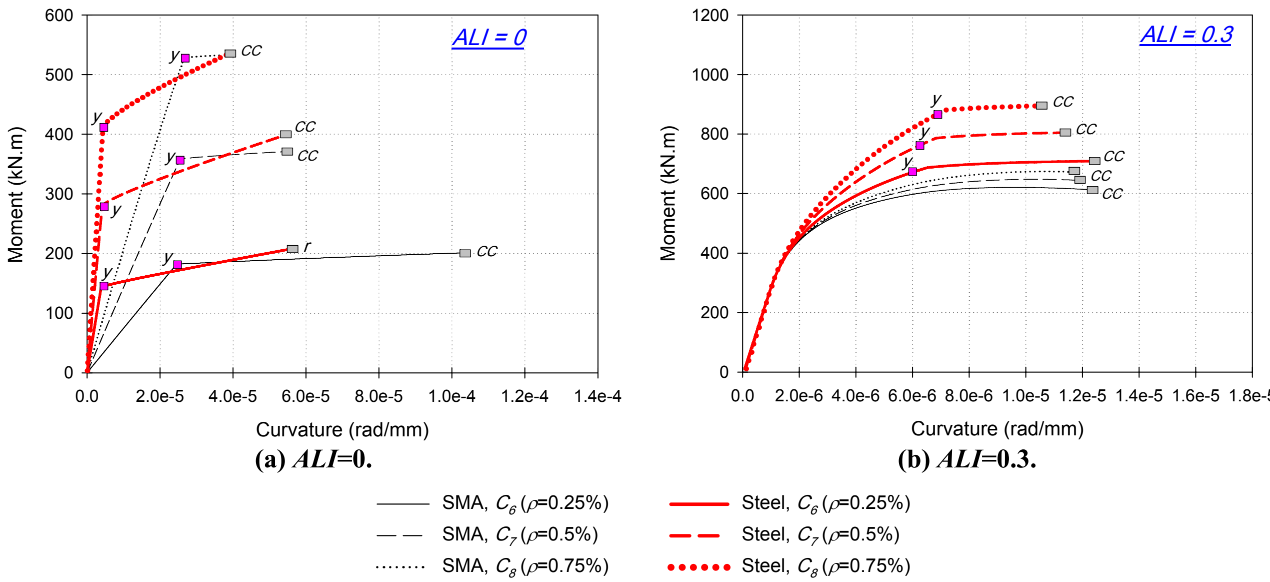

Fig. 6: Effect of varying ρ on the M-Φ relationship.

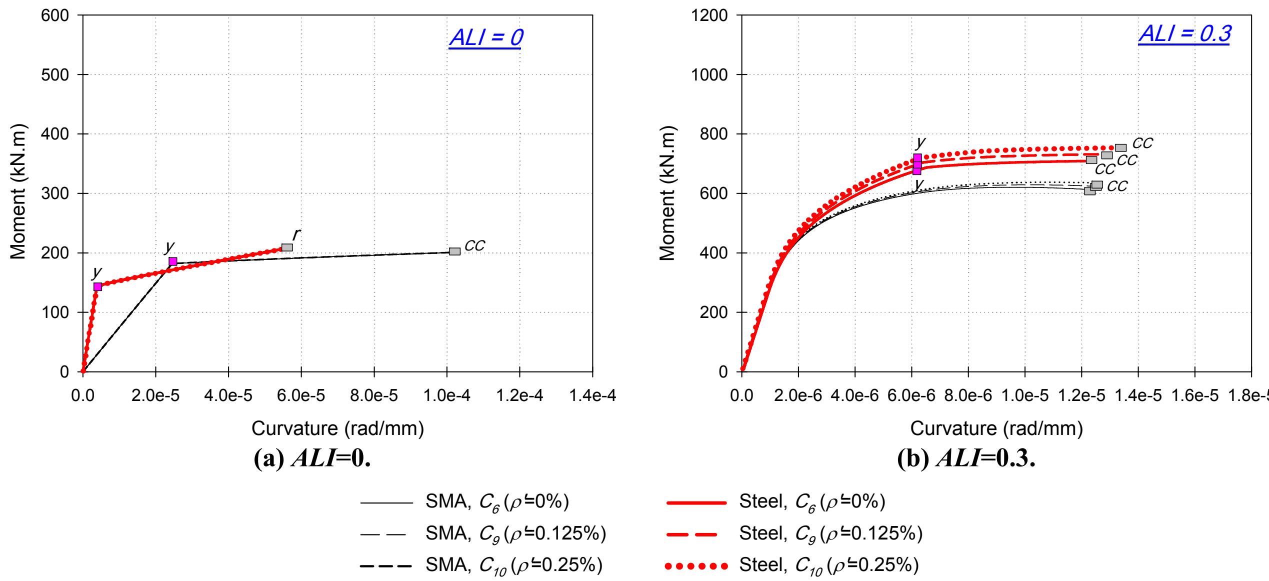

(a) *ALI*=0. **(b) *ALI*=0.3.**

Fig. 7: Effect of varying ρ' on the *M-Φ* relationship.

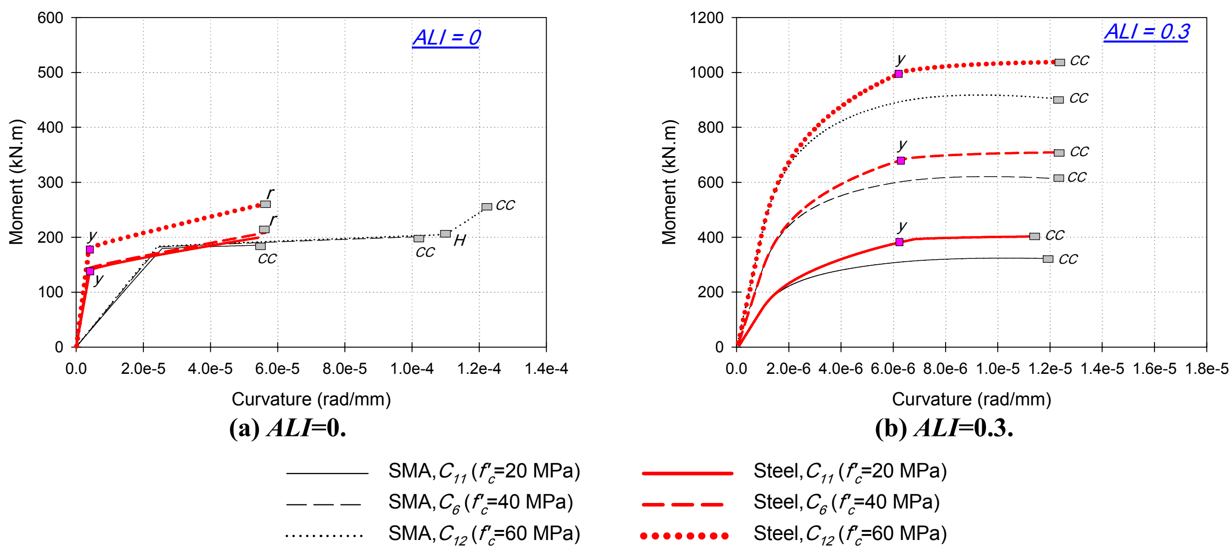

(a) *ALI*=0. **(b) *ALI*=0.3.**

Fig. 8: Effect of varying $f_c^{'}$ on the *M-Φ* relationship.

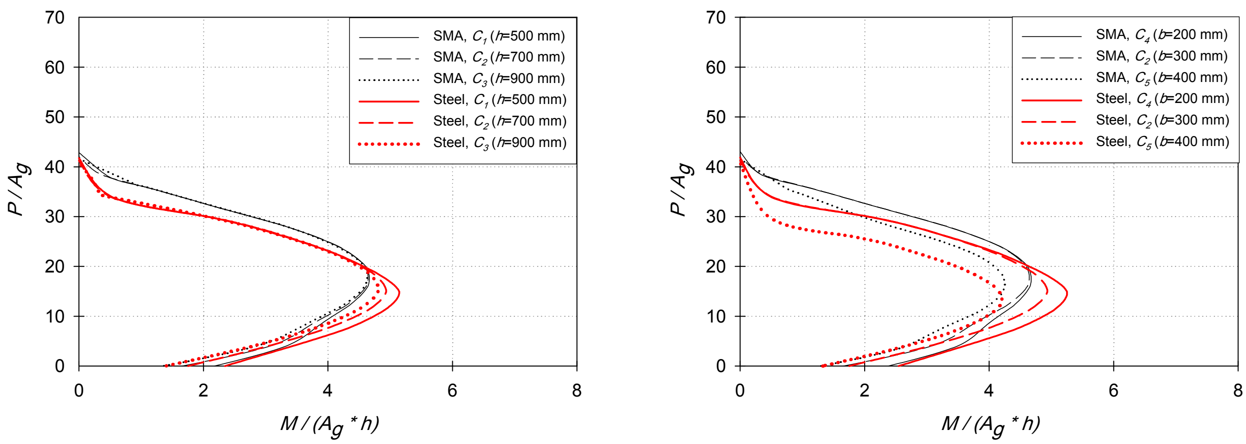

(a) *h*. **(b) *b*.**

Fig. 9: Effect of varying *h* and *b* on the normalized interaction diagram.

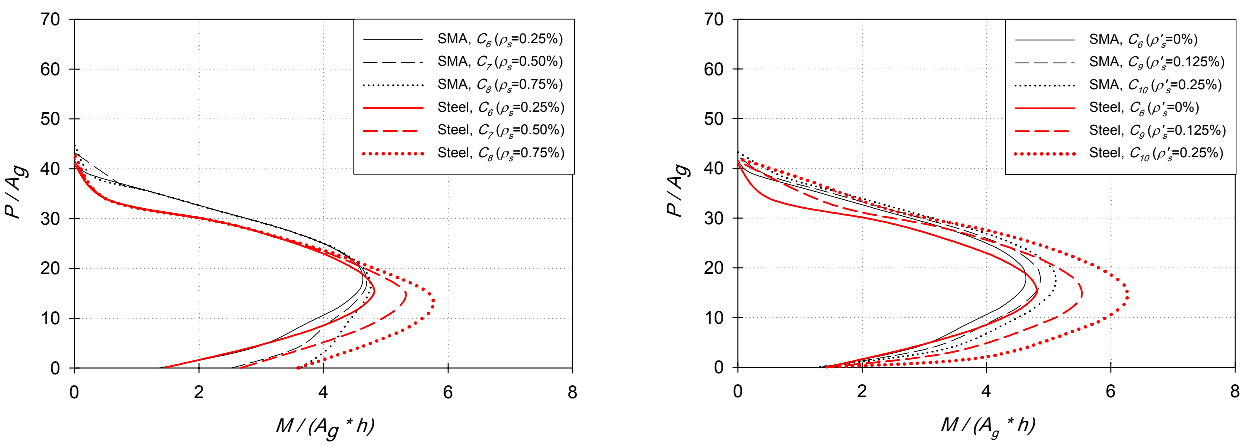

(a) ρ. **(b) ρ'.**

Fig. 10: Effect of varying ρ and ρ' on the normalized interaction diagram.

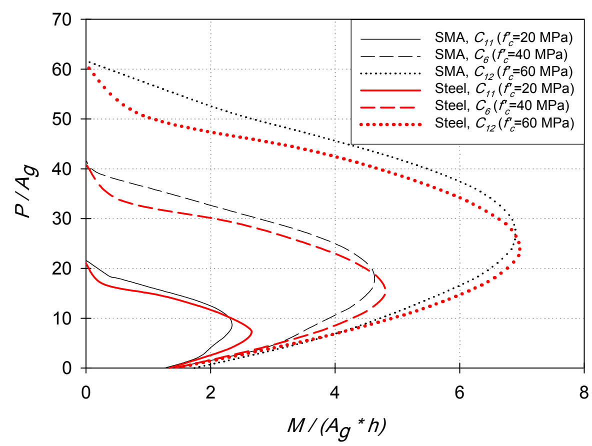

Fig. 11: Effect of varying f_c' on the normalized interaction diagram.

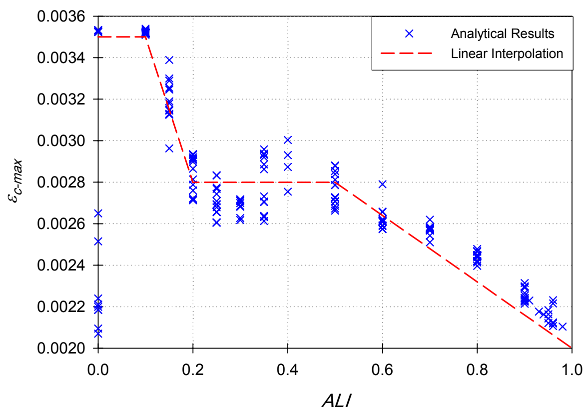

(a) $\varepsilon_{c\text{-}max}$ – *ALI* relationship.

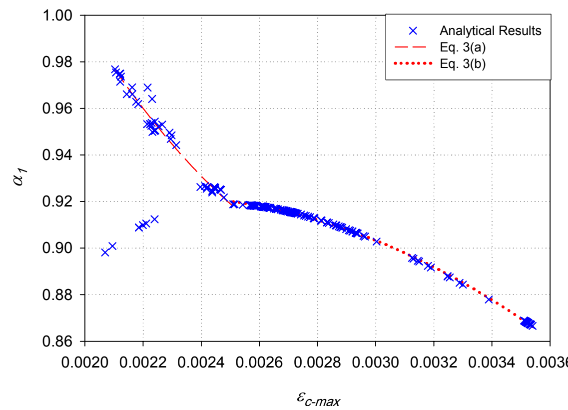

(b) α_1 – $\varepsilon_{c\text{-}max}$ relationship.

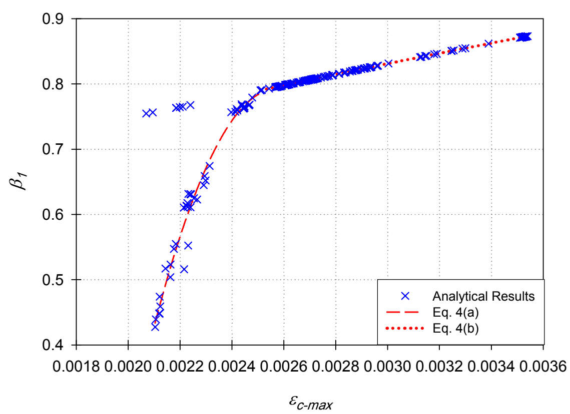

(c) β_1 – $\varepsilon_{c\text{-}max}$ relationship.

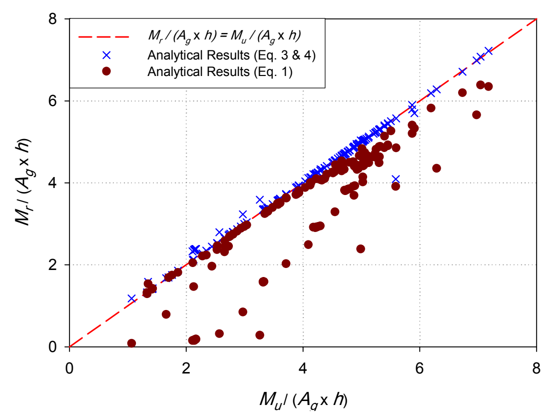

(d) M_r / (A_g x h) – M_u / (A_g x h) relationship.

Fig. 12: Steel RC sections.

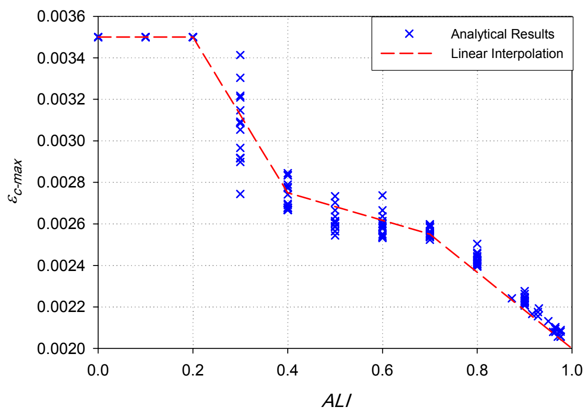

(a) $\varepsilon_{c\text{-}max}$ – *ALI* relationship.

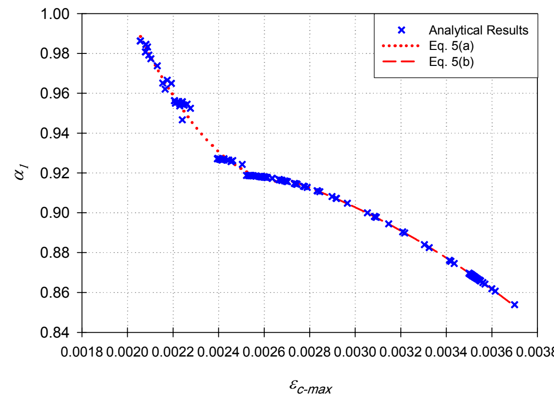

(b) α_1 – $\varepsilon_{c\text{-}max}$ relationship.

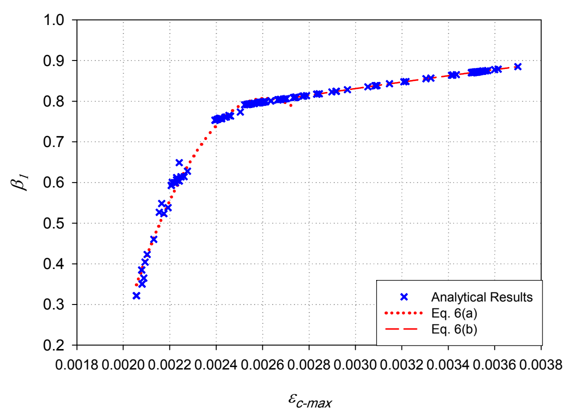

(c) β_1 – $\varepsilon_{c\text{-}max}$ relationship.

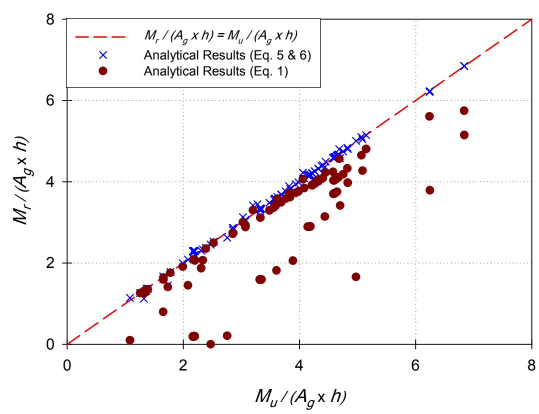

(d) M_r / (A_g x *h*) – M_u / (A_g x *h*) relationship.

Fig. 13: SMA RC sections.